Bound States in the Continuum and Induced Resonances in a Simple Plasmonic Waveguide with Sensing Application

Yamina Rezzouk, Soufyane Khattou, Madiha Amrani, Adnane Noual, El Houssaine El Boudouti, Abdelkrim Talbi, Bahram Djafari-Rouhani

To cite this version:

Yamina Rezzouk, Soufyane Khattou, Madiha Amrani, Adnane Noual, El Houssaine El Boudouti, et al.. Bound States in the Continuum and Induced Resonances in a Simple Plasmonic Waveguide with Sensing Application. Photonics, 2023, 10 (11), pp.1284. 10.3390/photonics10111284 . hal-04369666

HAL Id: hal-04369666
https://hal.science/hal-04369666v1

Submitted on 2 Jan 2024

photonics

MDPI

Article

Bound States in the Continuum and Induced Resonances in a Simple Plasmonic Waveguide with Sensing Application

Yamina Rezzouk [1,*], Soufyane Khattou [1], Madiha Amrani [1], Adnane Noual [1], El Houssaine El Boudouti [1], Abdelkrim Talbi [2] and Bahram Djafari-Rouhani [3,*]

[1] LPMR, Département de Physique, Faculté des Sciences, Université Mohammed I, Oujda 60000, Morocco; s.khattou@ump.ac.ma (S.K.); m1.amrani@ump.ac.ma (M.A.); a.noual@ump.ac.ma (A.N.); e.elboudouti@ump.ac.ma (E.H.E.B.)
[2] University of Lille, CNRS, Centrale Lille, Univ. Polytechnique Hauts-de-France, UMR 520-IEMN, F-59000 Lille, France; abdelkrim.talbi@univ-lille.fr
[3] IEMN, UMR CNRS 8520, Département de Physique, Université de Lille, 59655 Villeneuve d'Ascq, France
* Correspondence: rezzouk.yamina@ump.ac.ma (Y.R.); bahram.djafari-rouhani@univ-lille.fr (B.D.-R)

Abstract: A Friedrich–Wintgen bound state in the continuum (FW-BIC) is of particular interest in the field of wave physics phenomena. It is induced via the destructive interference of two modes that belong to the same cavity. In this work, we analytically and numerically show the existence of FW-BIC in a T-shaped cavity composed of a stub of length d_0 and two lateral branches of lengths d_1 and d_2, attached to an infinite waveguide. The whole system consists of metal–insulator–metal (MIM) plasmonic waveguides that operate in the telecommunication range. Theoretically, when d_1 and d_2 are commensurated, BIC is induced by these two branches. This latter is independent of d_0 and the infinite waveguide, where the T structure is grafted. By breaking the BIC condition, we obtain a plasmon-induced transparency (PIT) resonance. The PIT resonance's sensitivity to the dielectric material of the waveguide may be exploited to design a sensitive nanosensor suitable for sensing platforms, thanks to its very small footprint. A sensitivity of 1400 nm/RIU and a resolution of 1.86×10^{-2} RIU showed a high level of performance that the designed structure achieved. Moreover, this structure could also be used as a biosensor, in which we have studied the detection of the concentration in the human body, such as Na^+, K^+, and glucose solutions, and these sensitivities can reach 0.21, 0.28, and 1.74 nm dL/mg, respectively. Our designed structure advances with technology and has good application prospects, working as a biosensor to detect the blood's hemoglobin level. The analytical results, obtained via Green's function method, are validated via numerical simulations using Comsol Multiphysics software based on the finite element method.

Keywords: Friedrich–Wintgen bound states in the continuum; plasmon-induced transparency resonance; metal–insulator–metal waveguide; sensor

check for updates

Citation: Rezzouk, Y.; Khattou, S.; Amrani, M.; Noual, A.; El Boudouti, E.H.; Talbi, A.; Djafari-Rouhan, B. Bound States in the Continuum and Induced Resonances in a Simple Plasmonic Waveguide with Sensing Application. *Photonics* **2023**, *10*, 1284. https://doi.org/10.3390/photonics10111284

Received: 7 October 2023
Revised: 16 November 2023
Accepted: 17 November 2023
Published: 20 November 2023

1. Introduction

The term "plasmonics" refers to a branch of nanophotonics based on surface plasmons (SPs); it has triggered considerable research efforts during the last decade. A part of plasmonics is concerned with studying plasmonic waveguide propagation properties. Contrary to the usual photonic waveguides such as dielectric waveguides, plasmonic waveguides benefit from highly confined light beams in the sub-diffraction domain, with low propagation loss [1,2]. Surface plasmon polaritons (SPPs) are surface optical waves that propagate along the metal–dielectric interface [3], which makes them appealing for several applications in the nanoscale range [4–6]. Moreover, SPPs are deeply bonded to metal–insulator interfaces, with a penetration magnitude of an order of 100 nm into dielectrics and with approximate skin depths of 10 nm–20 nm into the metal, depending on the frequency range. SPPs have an intriguing ability that makes them strong candidates for the construction of integrated optical circuits in the sub-wavelength domain; indeed, this ability is to control light propagation properties [7,8]. Among the extensively investigated plasmonic structures, the metal–insulator–metal (MIM)-type waveguides have been studied rigorously for the realization of integrated optical circuitry [9] because of their ability to generate SPPs with long propagation lengths [10], high-group velocity over a wide bandwidth [11], and their inexpensive manufacturing costs [12]. MIMs are plasmonic nanosized structures in which a dielectric is enclosed by two metals. Furthermore, the simple design, the small size, and the capability to confine light at a deep subwavelength are the key features of the MIMs; hence, they are suitable for commercial disposition while preserving the sensor performance. Also, it is established that the sensitivity of MIM waveguides is higher than multilayers [13]. These plasmonic devices incorporate filters [14], sensors [15], demultiplexers [16], Mach–Zehnder interferometer (MZI) [17], and applications in highly integrated optical circuits [18]. Experimentally, MIM plasmonic waveguides have been implemented to observe plasmon-induced transparency (PIT) [19] and Fano resonances [20] in the visible and infrared domain using silver (Ag) or gold (Au) as the metal layer [21–23].

Recently, there has been a surge of interest in bound states in the continuum (BICs) [15,24] that have revolutionized nanostructures by providing the way to high-throughput optical sensing devices with enhanced light–matter interaction at the nanoscale [25–31]. BICs [32] are special types of resonant modes with an infinite lifetime that are still confined in certain parts of the system even though their frequencies lie in the radiative area. Three main types may be distinguished among the physical mechanisms underlying the generation of BICs [24]: BIC protected via symmetry or separability (SP-BIC) [33], Friedrich–Wintgen (FW) BIC [34], and Fabry–Perot (FP) BIC [35]. SP-BICs refer to symmetry incompatibility between two sets of modes; namely, a bound state with one symmetry class may fall into a continuum state with another class of symmetry without any coupling between them. FP-BICs refer to destructive interference when the spacing between two resonant cavities is tuned to make the round-trip phase shift add up to an integer multiple of 2π, causing destructive interference between the two resonances and then the formation of a BIC. FW-BIC is induced via the interaction of two interacting resonant modes within the same cavity. The resonances leading to the FW-BIC are coupled via the same radiation channel. Moreover, by tuning particular parameters, these modes approach each other, their interference induces an avoided crossing of the two resonances, and, at a specific value of the parameter, one resonance's width vanishes, giving rise to an FW-BIC, while the other mode becomes more lossy with a maximal width [36]. The FW-BICs were first proposed in quantum physics [34] and have since been extended to photonics [37] and plasmonics [38]. The most notable feature of BICs is the occurrence of high-quality quasi-BICs in the transmittance spectrum [39]. Further, the quasi-BIC emerges by tuning some parameters to make it slightly detuned from the critical coupling condition, so the otherwise localized BIC can couple with the incident wave [40]. The quasi-BIC can take the form of a PIT or Fano resonance with a finite width. The spectral position of these narrow resonances is affected by the refractive index of the surrounding medium, allowing for the design of optical sensors [41,42]. The capacity of sensors to identify material changes in the surrounding medium fundamentally determines how well they operate. Furthermore, the distinguishing features of a good sensor are the narrow resonance, high sensitivity (S), and high figure of merit (FOM). Zafar et al. analyzed a plasmonic refractive index (RI) sensor using a MIM waveguide with two stubs with a sensitivity of 1060 nm/RIU [43]; Wang et al. established a T-shaped MIM waveguide sensor with a sensitivity of 680 nm/RIU [44]; Yi et al. studied a U-shaped cavity MIM waveguide sensor with a sensitivity of 1000 nm/RIU [45]; while Adhikari et al. proposed a sensor based on the H-shaped MIM waveguide with a sensitivity of 1007.78 nm/RIU [46]. RI sensors have many applications in the biological and chemical fields, such as solution concentration which can be measured via RI changes [47–52].

In a recent paper [53], we studied photonic BIC and electromagnetic-induced transparency (EIT) resonances in a loop coupled laterally to a waveguide. Here, we show that a very simple plasmonic T-shaped cavity can produce BICs as well as PIT resonances with sensing applications. Although a T-cavity has been proposed in plasmonics for studying PIT resonances in simple [54] and periodic [55] nanodevices, to our knowledge, there is no study about FW-BICs in such a cavity with an application for sensing in the infrared domain. In this work, we analytically and numerically show the presence of FW-BIC in a T-shaped cavity made up of a stub of length d_0 and two lateral branches of lengths d_1 and d_2 (Figure 1). First, the transmission coefficient and the conditions that lead to FW-BICs are demonstrated analytically. Also, we show that taking the d_1 and d_2 commensurate is necessary for BIC to exist. This BIC is unaffected by d_0 and the infinite waveguide to which the cavity is connected. Moreover, we demonstrate that a slight deviation from the BIC position in the transmission spectra converts the latter into a PIT resonance. Then, we give an application of the plasmonic cavity for gas and biosensing in the infrared domain. It is worth noticing that Ag has been employed as a plasmonic metal in most numerical investigations of plasmonic RI sensors [43–46], while Au has been used in some experimental realizations of MIM waveguides [21,22]. However, our analytical results remain valid for either Ag or Au plasmonic waveguides. The theoretical results, obtained via Green's function method [56], are compared to the numerical simulations using Comsol Multiphysics software.

The paper is organized as follows: Sections 2 and 3 give the theoretical and numerical study of the transmission spectra into the T-shaped plasmonic cavity (Figure 1), as well as the conditions that lead to FW-BICs. Section 4 presents applications for gas sensing and biosensing when silver is used as the metal. The conclusion is presented in Section 5. The numerical results when gold is used as the metal instead of silver are given in Appendix A.

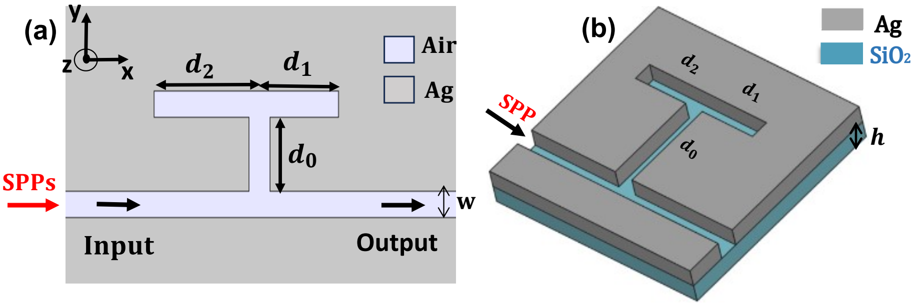

Figure 1. (**a**) 2D schematic diagram of a plasmonic T-shaped cavity based on MIM waveguides. The waveguide width is indicated by the notation w, which is equal to 50 nm. (**b**) 3D stereogram of the T-structure.

2. Basic Model and Theoretical Study

The studied system here is a plasmonic T-cavity composed of a stub with length d_0 and two lateral branches with lengths d_1 and d_2, attached to an infinite MIM waveguide. We assume that the whole system is filled with air ($\varepsilon_d = 1$), and the metal that surrounds it is made of silver (Ag), whose dielectric constant ε_m is given via the lossy Drude model [1]:

$$\varepsilon_m = \varepsilon_\infty - \frac{\omega_p^2}{\omega^2 + j\gamma\omega}, \tag{1}$$

where $\varepsilon_\infty = 3.7$ is the relative permittivity at infinite frequency, $\omega_p = 1.38 \times 10^{16}$ rad/s is the plasma frequency, $\gamma = 2.634 \times 10^{13}$ rad/s is the collision frequency, and ω is the angular frequency of the incident wave. These values are suitable for the experimental findings in the infrared domain (700 nm < λ < 6000 nm) [57]. Moreover, $\gamma = 1/\tau$ accounts for the losses in the metal due to the damping of the vibrating electrons, where τ is the relaxation time. Indeed, Ag has been extensively employed in MIM waveguides since it uses less power and has lower absorption than other plasmonic metals [47]. We consider the SPPs as hybrid modes, comprising the features of both the propagating electromagnetic waves in dielectrics, which are transverse waves, and free electron (plasma) oscillations in metals, which are longitudinal. Since the TE (transverse electric) waves are purely transverse, with only H_x, H_y, and E_z being non-zero, they cannot be coupled to the longitudinal electron oscillations in metals. Hence, we consider only the TM (transverse magnetic) waves, where only the field components E_x, E_y, and H_z are nonzero, corresponding to the SPP modes in the MIM waveguides. Further, the waveguide and the T-shaped cavity are taken as identical with a width w of 50 nm to ensure that only the transverse magnetic mode TM_0 exists in the MIM plasmonic waveguide; hence, the waveguide width w shall be extremely narrow compared to the plasmon wavelength w $\ll$ λ_{sp}. The plasmonic device presented in Figure 1a is a 2D model in the (x,y) plane and infinite in the z-direction. This design is the most used geometry in MIM waveguide simulations as it is less time consuming than the fully realistic 3D MIM waveguides (Figure 1b), which have a finite height h in the z-direction and are deposited on a SiO_2 substrate. However, it was shown that, beyond a specific h value ($h = 50$ nm), the 2D and 3D models provide almost similar results in regard to the positions, shapes, and widths of the resonant modes in the transmission spectra [58,59]. In addition, the benefit of using the 1D approach resides in the analytical calculations' derivation, which enables us to understand the origin of each mode propagating in such structures. Nevertheless, it is necessary to include the SPP propagation wavevector k_{sp} and the impedance Z along the waveguide before using Green's function approach adjusted to the 1D MIM waveguides. It is shown that whenever the separating space between two interfaces is comparable to the decay lengths of SPPs in the dielectric region, the SPPs become coupled to each other and remain confined in the dielectric region between two metals. The wavevector k_{sp} can be obtained from the dispersion relation of the symmetric eigenmodes of the MIM waveguide, where one can easily show after a Taylor expansion that [1]

$$k_{sp} = k_0\sqrt{\varepsilon_d - \frac{2\varepsilon_d\sqrt{\varepsilon_d - \varepsilon_m}}{\varepsilon_m k_0 \mathrm{w}}}, \tag{2}$$

where $k_0 = \frac{\omega}{c}$ is the wavevector in vacuum and c is the speed of light in vacuum.

The second interesting quantity concerns the impedance Z of the MIM waveguide. By applying the transmission line theory [60], the impedance Z is approximately given by the first-order Taylor expansion as [1]

$$Z = \frac{k_{sp}\mathrm{w}}{\varepsilon_d \omega}. \tag{3}$$

The geometric parameters of the T-cavity are chosen so that d_0 and d_1 are fixed at 540 nm and 270 nm, respectively, whereas d_2 is taken as a variable to operate in the infrared range and close to the telecommunications region.

The calculation method employed in this study is obtained using Green's function [56], allowing us to deduce the transmission coefficient and the isolated cavity's eigenmodes with various boundary conditions at the ends of the lateral guides. The analytical results are validated via numerical simulations using Comsol Multiphysics software in MIM plasmonic waveguides. The transmission coefficient for the T structure can be obtained in the same way as in Ref. [53] that,

$$t = \frac{\tau}{\tau + j\rho}, \tag{4}$$

where τ and ρ are given by

$$\tau = 2[C_0 - S_0(A_1 + A_2)] \tag{5a}$$

and

$$\rho = S_0 + C_0(A_1 + A_2). \tag{5b}$$

$C_i = \cos(k_{sp}d_i)$, $S_i = \sin(k_{sp}d_i)$, $A_i = \frac{ZS_i + jZ_mC_i}{ZC_i - jZ_mS_i}$ $(i = 0, 1, 2)$, $Z_m = \frac{k_m w}{\varepsilon_m \omega}$ and $k_m = k_0\sqrt{\varepsilon_m}$.

It is well known [61,62] that the eigenmodes of the isolated cavities with either vanishing magnetic field H = 0, called the Neumann boundary condition (NBCS), or vanishing electric field E = 0, called the Dirichlet boundary condition (DBCS), at the end of d_0 can be deduced, respectively, from the reflection and transmission coefficients' zeros; (i.e., from vanishing the expression of τ (Equation (5a)) and ρ (Equation (5b)), respectively); when this cavity is grafted to an infinite waveguide (Figure 1a), namely,

$$\tau = 0 \tag{6a}$$

and

$$\rho = 0. \tag{6b}$$

On the other hand, the eigenmodes of the whole system (Figure 1a) when the cavity is attached to the waveguide could be determined from the poles of Green's function or else by vanishing the denominator of the transmission coefficient (Equation (4)), that

$$\tau + j\rho = 0. \tag{7}$$

Due to the radiation in the waveguide, these modes have complex frequencies. BIC occurs when the real (Equation (6a)) and imaginary (Equation (6b)) parts vanish at the same frequency, which would mean a mode without radiation or an infinite lifetime. However, to find the analytical expressions that lead to the BIC conditions, we should first neglect the loss in the materials. Therefore, the solution of Equation (7) yields the following simple equations and, thereby, to a BIC:

$$C_1 = 0 \quad and \quad C_2 = 0. \tag{8}$$

In a lossless system, when $Im(k_{sp}) = 0$, the solutions of Equation (8) are given by $k_{sp}d_1 = (2m_1 + 1)\frac{\pi}{2}$ and $k_{sp}d_2 = (2m_2 + 1)\frac{\pi}{2}$. So, one can deduce the commensurability between d_1 and d_2

$$\frac{d_2}{d_1} = \frac{2m_2 + 1}{2m_1 + 1}, \tag{9}$$

where m_1 and m_2 are integers. In what follows, for the sake of simplicity, we take $m_1 = m_2 = 0$ (i.e., $d_1 = d_2$). In this case, the expression of the transmission becomes

$$t = \frac{2S_0}{2S_0 - jC_0}. \tag{10}$$

From Equation (10), one can deduce the transmission rate

$$T = |t|^2 = \frac{4S_0^2}{3S_0^2 + 1}. \tag{11}$$

The latter equation (Equation (11)) shows clearly that the transmission rate is finite at the BIC frequencies and varies between zero (for $S_0 = 0$) and unity (for $S_0 = \pm 1$).

3. Numerical Analysis

In order to visualize the behavior of the BICs, we give in Figure 2a,b the analytical and numerical simulations of the transmission magnitude in color scale as a function of the wavelength and d_2 for the fixed lengths of d_0 and d_1 (i.e., $d_0 = 2d_1 = 540$ nm and $d_1 = 270$ nm). Furthermore, these values have been chosen so that the result falls close to the telecom wavelength of 1.5 µm. The analytical results shown in Figure 2a are obtained using Green's function method. As a matter of comparison, we present in Figure 2b the results of the numerical calculations obtained by using Comsol Multiphysics software. A good agreement can be noticed between both results. We can observe the narrowing of the resonance, then its transformation into an FW-BIC at λ =1528 nm for d_1 = d_2 = 270 nm. The white circles represent the FW-BIC's positions. A transparency window between two zeros appears when we deviate slightly from the BIC condition, giving rise to PIT resonance. To give a better overview of the behavior of the FW-BIC as well as the corresponding PIT resonances, we plotted in Figure 2c the transmission spectra as a function of the wavelength for three values of d_2. The blue solid lines indicate the analytical findings, whereas the red open circles represent the numerical simulations. The peak between the two transmission zeros gives rise to a well-defined PIT resonance. This resonance becomes increasingly narrow as d_2 increases; at d_2 = d_1, the width of this resonance disappears, giving rise to FW-BIC at λ=1528 nm, which is denoted by the black arrow. The BIC becomes an asymmetric PIT resonance as we shift out from the BIC position. It is clear that the transmission falls short of unity (T_{max} = 0.8) as an outcome of metal losses. We have reported in Figure 2d the eigenmodes with the Dirichlet (τ_{min}, pink curve) and Neumann (ρ_{min}, cyan curves) boundary conditions at the end of d_0, as a function of the stub d_2. The cyan and pink curves are taken from the maxima and minima of the transmission spectra in Figure 2c, respectively. Moreover, the crossing between two DBCS modes and one NBCS mode gives rise to an FW-BIC at λ =1528 nm for d_2 = 270 nm. By deviating from the BIC position, the FW-BIC transforms into a resonance (cyan branch) between two transmission zeros (pink branches). We present in Figure 2e the full width at half maximum (FWHM) for the lower (blue curve) and upper (red curve) transmission dips as a function of d_2, to better explain the evolution of the two dips' linewidth in Figure 2c. The linewidth of the upper dip (γ_-) decreases and vanishes at d_2 = 270 nm, giving rise to an FW-BIC. On the other hand, the FWHM of the lower dip (γ_+) increases and becomes wider at d_2 = 270 nm. The behavior of the widths γ_- and γ_+ of the two interacting modes in Figure 2e is a characteristic of the FW-BIC [34].

The spatial field associated with the FW-BIC and the PIT resonance within the cavity depends on the position where the excitation is applied. Figure 2f–h displays the magnetic field localization (H_z-field map) at λ = 1528 nm (for d_1 = d_2 = 270 nm), λ=1480 nm (for d_1 = 270 nm and d_2 = 240 nm), and λ = 1635 nm (for d_1 = 270 nm and d_2 = 300 nm) when the local magnetic excitation source is applied at the border of the waveguide of length d_1 (indicated by the red arrow), respectively. We can clearly see that the BIC (Figure 2f) is tightly confined within the two lateral guides and does not radiate outside of them. This mode is a stationary wave in the lateral cavity, where the corresponding magnetic field vanishes at the intersection of the two guides of lengths d_1 and d_2 and the vertical stub of length d_0, giving rise to an anti-symmetric mode. Likewise, Figure 2g,h shows the H_z-field map of the PIT resonances (quasi-BIC), in which the mode exhibits some leakage into the T-cavity and the main waveguide; however, the field in the lateral guides remains higher and close to that of the BIC. Now, by applying the local magnetic excitation source along the main horizontal waveguide, we obtain different results for the localization of the H_z-field map, as shown in Figure 2i–k. Here, the BIC in the lateral cavity (Figure 2i) cannot be excited from the main waveguide as it is decoupled from the latter and, therefore, the magnetic field spreads along the whole system with a vanishing magnetic field at all the connecting points of the finite guides. Also, this mode is prohibited from transmission as it corresponds to a zero transmission. However, as soon as the BIC transformed into a quasi-BIC (Figure 2j,k), a field similar to that of the BIC appears inside the lateral cavity. These findings demonstrate that, depending on the geometrical parameters, the true BIC can be observed by applying an excitation magnetic field inside the cavity (Figure 2i) or by transforming the BIC to a quasi-BIC and applying the excitation either inside the cavity (Figure 2g,h) or from the main waveguide (Figure 2j,k). Also, the T-cavity may be used as a selective or rejective filter for specific wavelengths.

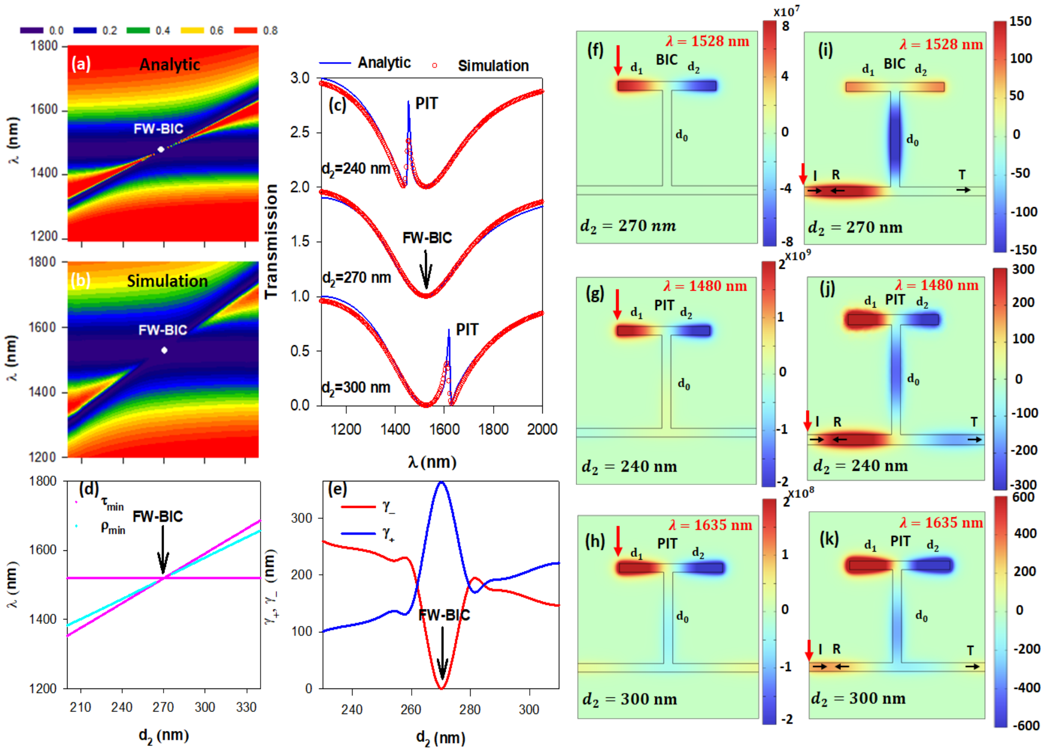

Figure 2. (**a**,**b**) Analytical and numerical variation in the transmission magnitude versus the wavelength and d_2, for d_0 = 540 nm and d_1 = 270 nm. (**c**) Transmission spectra as a function of the wavelength for various values of d_2. The blue and red curves indicate the analytical and numerical results, respectively. (**d**) Eigenmodes of the isolated cavity, with Dirichlet (τ_{min}, pink curve) and Neumann (ρ_{min}, cyan curves) boundary conditions at the end of d_0, versus the stub of length d_2. (**e**) Linewidth of the lower (blue curve) and upper (red curve) transmission dips. The white circles in (**a**,**b**) and the black arrows in (**c**–**e**) indicate FW-BIC's positions. (**f**) Magnetic (H_z) field map of the FW-BIC at λ = 1528 nm for d_2 = 270 nm excited via local magnetic excitation at the border of the horizontal guide of length d_1. (**g**,**h**) H_z-field map of the PIT resonances at λ = 1480 nm for d_2 = 240 nm and λ = 1635 nm for d_2 = 300 nm, respectively. (**i**–**k**) H_z-field maps of the BIC and the PIT resonances excited by an incident wave at the left semi-infinite waveguide. The position of the excitation is shown by the red arrow in (**f**–**k**).

In the following, we will discuss the transmission when the parameter d_0 is taken as a variable. To visualize the behavior of FW-BICs and the corresponding PIT resonance, we plotted in Figure 3a,b the theoretical transmission magnitude in color scale as a function of the wavelength and d_0, for $d_1 = d_2$ = 270 nm and d_1 = 270 nm and d_2 = 300 nm, respectively. As predicted, for $d_1 = d_2$ = 270 nm (Figure 3a), the BIC remains constant as a function of d_0 at λ = 1528 nm, represented by a horizontal dashed line. As we can see, with increasing d_0, the amplitude of the transmission at λ = 1528 nm progressively decreases and then increases following Equation (11). For d_1 = 270 nm and d_2 = 300 nm (Figure 3b), the FW-BIC turns into a PIT resonance, which appears as a transparency window between two transmission zeros.

Moreover, Figure 3c,d presents two transmission spectra, in the case of FW-BIC (Figure 3a), for d_0 = 570 nm and d_0 = 650 nm, respectively. Thus, the BIC appears with an amplitude T = 0.1 for d_0 = 570 nm (Figure 3c) and with an amplitude of 0.63 for d_0 = 650 nm (Figure 3d). Accordingly, the results found here confirm the analytical calculations previously shown in Equation (11). Moreover, in Figure 3e,f, we give two transmission spectra for d_0 = 570 nm and d_0 = 650 nm, respectively, in the case of a PIT resonance (Figure 3b). Depending on the value of d_0, a PIT resonance occurs between two transmission zeros either symmetrically (Figure 3e) or asymmetrically (Figure 3f). The blue solid lines represent the analytical results, while the red open circles show the numerical simulations.

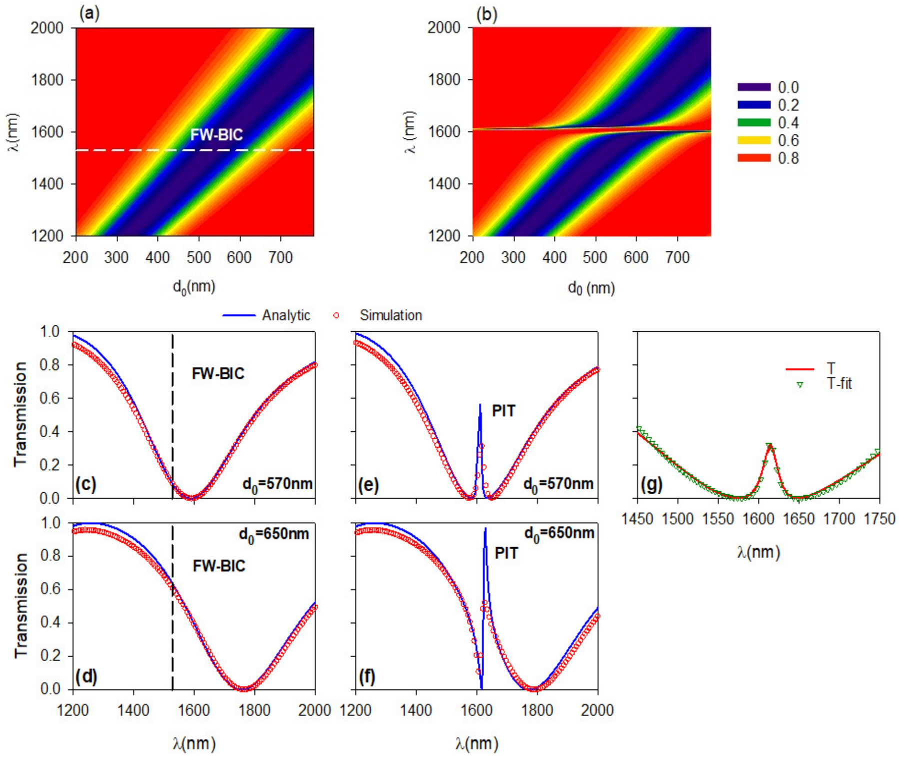

Figure 3. Analytical variation in the transmission magnitude versus the wavelength and d_0, for (**a**) d_1 = d_2 = 270 nm, and (**b**) d_1 = 270 nm, d_2 = 300 nm. The white dashed line in (**a**) at λ = 1528 nm indicates FW-BIC's position as a function of d_0. Transmission spectra as a function of the wavelength for d_1 = d_2 = 270 nm, and (**c**) d_0 = 570 nm, (**d**) d_0 = 650 nm, respectively. Transmission spectra as a function of the wavelength for d_1 = 270 nm, d_2 = 300 nm, and (**e**) d_0 = 570 nm, (**f**) d_0 = 650 nm, respectively. The blue and red curves indicate the analytical and numerical results, respectively. (**g**) Exact (solid line) and fit (green open triangles) results of the PIT resonance for d_0 = 570 nm presented in (**e**).

In order to ensure that the transmission resonance in Figure 3e exhibits a PIT shape, we have presented in Figure 3g the fitted curve (green open triangles) following the PIT form [16]

$$T = A\frac{(\lambda - \lambda_{res} + q_1\Gamma)^2(\lambda - \lambda_{res} + q_2\Gamma)^2}{(\lambda - \lambda_{res})^2 + \Gamma^2}, \tag{12}$$

where $A = \frac{1}{q_1 q_2 \Gamma}$, q_1, and q_2 are the Fano parameters describing the degree of the asymmetry of both resonances, λ_{res} is the resonance wavelength, and Γ is the FWHM of the PIT resonance. In Figure 3e, the approximate results (green open triangles) obtained from Equation (12) fit well with the exact findings (red line) and show that the resonance is a PIT-like resonance with $q_1 = -3.6$, q_2 = 3.8 and Γ = 9.85 nm.

4. Sensing Applications

The proposed plasmonic structure can be used as a refractive index sensor when the index of the surrounding medium is changed. The sensing principle is based on monitoring the shift in the resonance wavelength for changing the RI of the material [47]. Thus, this sensor configuration has the advantage of an ultra-compact size and high sensitivity.

4.1. Gas Sensing

The sensitivity (S) is a key parameter to measure the performance of a sensor. It can be defined as the shift in the resonance wavelength ($\Delta\lambda_{res}$) per unit change in the RI (Δn), such that

$$S = \frac{\Delta\lambda_{res}}{\Delta n}. \tag{13}$$

Another important quantity is the detection limit (DL), which enables measuring the performance of plasmonic sensors [63]. Here, we introduce the concept of sensor resolution, which characterizes the small change in the RI that can be measured in the sensor output,

$$DL = \frac{\Gamma}{S}. \tag{14}$$

In the following, we consider a plasmonic sensor, where we keep the structural parameters described in Section 3 unchanged while varying the RI of the waveguide. Moreover, we take the PIT resonance, which occurs at $\lambda = 1480$ nm ($d_2 = 240$ nm), to be the resonance under study for the sensitivity of our system. Figure 4a illustrates the transmission spectra for the changed RI from $n = 1$ to $n = 1.1$ with a step of 0.02.

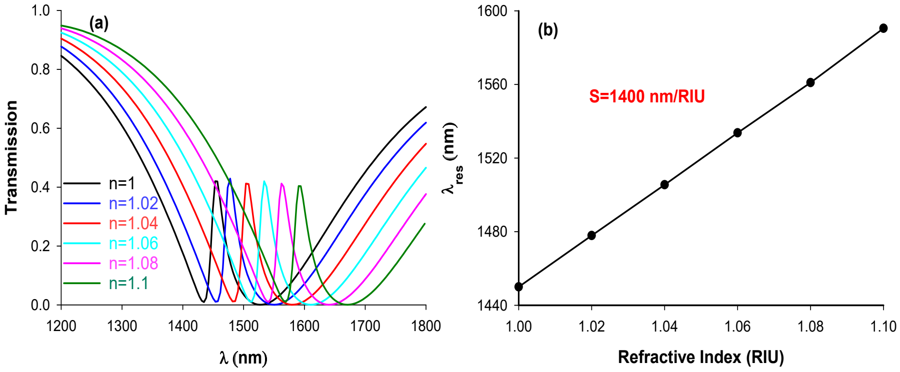

Figure 4. (**a**) Transmission spectra as a function of the wavelength for various refractive indexes n. (**b**) The variation in resonant wavelength λ_{res} versus the RI.

There is a redshift and a linear correlation with increasing n, as seen in the transmission peaks. Figure 4b shows the evolution of the resonance wavelength (λ_{res}) presented in Figure 4a as changing the refractive indexes n. One can observe a linear relationship between λ_{res} and n by changing n from 1 to 1.1. From this curve's slope, we deduce a sensitivity of $S = 1400$ nm/RIU and a resolution of $DL = 1.86 \times 10^{-2}$ RIU.

Table 1 compares our sensitivity results to those from some similar MIM plasmonic RI sensors in the literature. Our device exhibits an improved sensitivity, compared to other RI sensors.

Table 1. Sensitivity comparison of some recently reported plasmonic RI sensors with our work.

Design Structure	Sensitivity (nm/RIU)	Resonance Wavelength (nm)	Reference
MIM waveguide with two stubs	1060	1000	[43]
T-shaped MIM waveguide	680	682	[44]
U-shaped cavity MIM waveguide	1000	1064	[45]
H-shaped MIM waveguide	1007.78	1313	[46]
Our design	1400	1480	- -

4.2. Biosensing

Our MIM plasmonic structure can also be used as a biosensor to measure the concentration of unknown samples from human blood [15,49,50]. In this section, we use our cavity to measure certain electrolytes in human blood samples, including Na^+, K^+, and glucose. The biosensor's remaining geometrical parameters are identical to that employed in the preceding part (Section 4.1). The refractive index and the concentration of the sample have a well-established relationship [48,52], which is as follows:

$$n_{Na^+} = 1.3373 + 1.768 \times 10^{-3}(\frac{Ck}{393}) - 5.8 \times 10^{-6}(\frac{Ck}{393})^2, \tag{15}$$

$$n_{K+} = 1.3353 + 1.6167 \times 10^{-3} (\frac{Ck}{529.8}) - 4 \times 10^{-7} (\frac{Ck}{529.8})^2, \quad (16)$$

$$n_{Glucose} = 0.00011889Ck + 1.33230545. \quad (17)$$

Here, C stands for concentration in mg/dL, and k is the concentration factor that takes the values of 30, 50, and 10 for Na^+, K^+, and glucose, respectively.

A biosensor's performance is defined by its sensitivity S' to the concentration shifts, as described by

$$S' = \frac{\Delta\lambda}{\Delta C}. \quad (18)$$

The surrounding waveguides of the suggested biosensor are filled with various concentrations of Na^+, K^+, and glucose to evaluate the detection performance at the optimal structural configuration. Moreover, the concentrations of the Na^+, K^+, and glucose solutions were set to be 200 to 440 mg/dL with a 60 mg/dL interval, 0 to 80 mg/dL with a 20 mg/dL interval, and 110 to 230 mg/dL with a 30 mg/dL interval, respectively. As the concentrations are changed, the transmittance curves shown in Figure 5a–c reveal discernible transmission peak changes, along with an increase in the resonance wavelengths. The shifts of the resonances exhibit a linear behavior, as in the insets of Figure 5a–c. Furthermore, a maximum sensitivity of 0.21, 0.28, and 1.74 nm dL/mg have been recorded from the slopes of these curves for the Na^+, K^+, and glucose solutions. Such changes in the transmittance peaks may be easily detected, giving our suggested biosensor the benefit of being a straightforward and inexpensive nanoscale device.

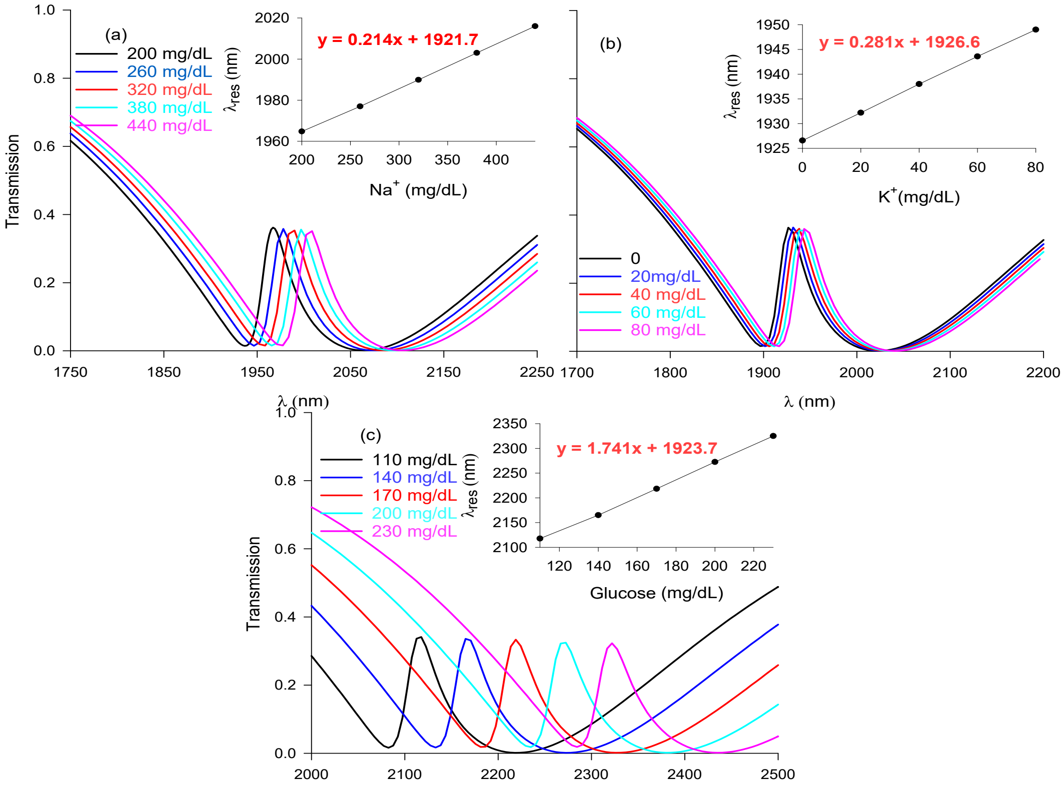

Figure 5. Transmission plots as a function of the wavelength for various concentrations C: (**a**) Na^+, (**b**) K^+, and (**c**) glucose solutions. The evolutions of resonant λ_{res} as a function of the concentrations C are depicted in the insets of (**a**–**c**).

5. Conclusions

We investigated analytically and numerically the FW-BICs in a MIM T plasmonic structure operating in the infrared domain. We demonstrated that taking the lengths of the two horizontal guides d_1 and d_2 and commensurating them is a requirement condition for obtaining BICs. Furthermore, we showed that by breaking the BIC condition, the BIC turns into a PIT resonance. By harnessing PIT resonances in the proposed T-shaped cavity system, we have shown the possibility of designing a highly sensitive sensor, which can be employed to detect small amounts of gases as well as the concentrations of the Na^+, K^+, and glucose solutions, in comparison with other plasmonic sensors. Furthermore, due to its small dimensions lying at the nanoscale, the proposed nanosensor can be easily integrated into the on-chip optical sensing platforms. Our results remain valid for either Ag or Au plasmonic metals as both metals are described by dielectric constants using the Drude–Lorentz model. Finally, let us mention that using waveguides based on structured metamaterials like magnetic photonic crystals with negative permeability as well as left-handed materials with negative permeability and permittivity can support magnetic surface plasmons [64–66] with BICs and PIT resonances for applications in the nonreciprocal waveguide and nonreciprocal scattering [67,68].

Author Contributions: Investigation, Y.R., S.K., M.A. and E.H.E.B.; software, Y.R. and S.K.; supervision, E.H.E.B. and B.D.-R.; writing—original draft, Y.R.; writing—review and editing, E.H.E.B., A.N., A.T. and B.D.-R. All authors have read and agreed to the published version of the manuscript.

Funding: This research received no external funding.

Institutional Review Board Statement: Not applicable.

Informed Consent Statement: Not applicable.

Data Availability Statement: The data presented in this study are available on reasonable request from the corresponding author.

Conflicts of Interest: The authors declare that there is no conflict of interest.

Appendix A. Numerical Results Based on Gold as a Metal

The plasmonic structure under study can be designed with the current manufacturing technologies. Furthermore, various papers proposed the fabrication of MIM plasmonic waveguide structures such as the stub structure [21], the plasmonic structure consisting of single and two nanocavities [22,69], and V-shaped grooves [70]. These structures are made up of air nanocavities that are 150 nm deep and engraved in a 300 nm thick gold film deposited on a SiO_2 substrate. A laser molecular beam epitaxy growing technique was used to fabricate the gold film. Each of the gold nanoparticles has a solid core linked to many, spike-shaped points that range between 10 and 20 nm in length. The light source was a beam output generated by using excimer laser system. The plasmonic microstructure was prepared using a focused ion beam etching method. Moreover, a decoupling grating with a depth of 150 nm had also been etched in the plasmonic waveguide's output port so as to help coupling the SPP mode into a free space for the purpose of measurement. The SPP mode was mostly confined in the nanocavity region and extended to the upper multi-component nanocomposite cover layer, indicating that the plasmonic nanogroove resonance modes are responsive to the changes in the multicomponent nanocomposite cover layer's refractive index. Likewise, the fabrication of our suggested design may be accomplished by placing a metallic Au film over a SiO_2 substrate, followed by the etching of the T-shaped cavity to produce the plasmonic MIM system. Therefore, this design makes it easier to create nanosized structures and may be utilized to analyze transmission properties in the Terahertz domain.

In this section, we show the possibility of observing the BIC and the PIT resonance using Au as a metal instead of Ag [21,22,69]. The dielectric constant of Au is described by the Drude–Lorentz model which has been taken from [71]. In Figure A1, we plotted the transmission spectra numerically for some values of d_2. However, we changed the width of the waveguides to be w = 150 nm in accordance with the experimental realizations [21,22,69].

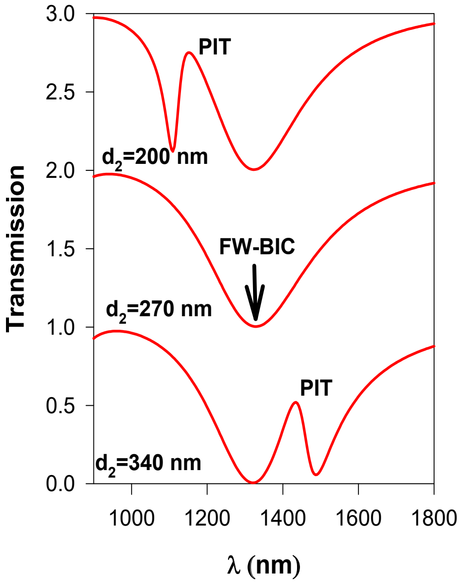

Figure A1. Numerical results of transmission spectra as a function of the wavelength for different d_2 values using gold as a metal.

Figure A1 shows the existence of PIT resonances and their transformation to the BIC, which occurs as a zero-width resonance at λ = 1330 nm for d_2 = 270 nm. These results show similar behavior as the plasmonic T-cavity using silver and confirm the applicability of our calculations to gold. However, the width of the PIT resonances in the transmission spectra is wider due to higher losses in gold than silver. Therefore, the quality factor, the sensitivity of the gas sensor and the biosensor become smaller when gold is used as the metal.

References

1. Maier, S.A. *Plasmonics: Fundamentals and Applications*; Springer: New York, NY, USA , 2007.
2. Ohashi, K.; Nishi, K.; Shimizu, T.; Nakada, M.; Fujikata, J.; Ushida, J.; Torii, S.; Nose, K.; Mizuno, M.; Yukawa, H.; et al. On-chip optical interconnect. *Proc. IEEE* **2009**, *97*, 1186–1198. [CrossRef]
3. Barnes, W.L.; Dereux, A.; Ebbesen, T.W. Surface plasmon subwavelength optics. *Nature* **2003**, *424*, 824–830. [CrossRef] [PubMed]
4. Oo, S.Z.; Silva, G.; Carpignano, F.; Noual, A.; Pechstedt, K.; Mateos, L.; Grant-Jacob, J.A.; Brocklesby, B.; Horak, P.; Charlton, M.; et al. A nanoporous gold membrane for sensing applications. *Sens. -Bio-Sens. Res.* **2016**, *7*, 133–140. [CrossRef] [PubMed]
5. Saada, T.N.; da Silva, A.G.M.; Subramanian, P.; Pang, L.; Noual, A.; Djafari-Rouhani, B.; Mishyn, V.; Meziane, D.; Melinte, S.; Sandu, G.; et al. Plasmon-enhanced electrocatalytic oxygen reduction in alkaline media on gold nanohole electrodes. *J. Mater. Chem. A* **2020**, *8*, 10395–10401. [CrossRef]
6. Fan, X. Sensitive surface plasmon resonance label-free biosensor on a fiber end-facet. *Light Sci. Appl.* **2022**, *11*, 325. [CrossRef] [PubMed]
7. Dombi, P.; Pápa, Z.; Vogelsang, J.; Yalunin, S.V.; Sivis, M.; Herink, G.; Schàfer, S.; GroB, P.; Ropers, C.; Lienau, C. Strong-field nano-optics. *Rev. Mod. Phys.* **2020**, *92*, 025003. [CrossRef]
8. Smirnov, V.; Stephan, S.; Westphal, M.; Emmrich, D.; Beyer, A.; Golzhauser, A.; Christoph, L.; Silies, M. Transmitting surface plasmon polaritons across nanometer-sized gaps by optical near-field coupling. *ACS Photonics* **2021**, *8*, 832–840. [CrossRef]
9. Dionne, J.A.; Sweatlock, L.A.; Atwater, H.A.; Polman, A.J.P.R.B. Plasmon slot waveguides: Towards chip-scale prop-agation with subwavelength-scale localization. *Phys. Rev. B* **2006**, *73*, 035407. [CrossRef]
10. Neutens, P.; Van Dorpe, P.; De Vlaminck, I.; Lagae, L.; Borghs, G. Electrical detection of confined gap plasmons in metal–insulator–metal waveguides. *Nat. Photon.* **2009**, *3*, 283–286. [CrossRef]
11. Han, Z.; Forsberg, E.; He, S. Surface plasmon Bragg gratings formed in metal-insulator-metal waveguides. *IEEE Photonics Technol. Lett.* **2007**, *19*, 91–93. [CrossRef]
12. Wen, K.; Yan, L.; Pan, W.; Luo, B.; Guo, Z.; Guo, Y.; Luo, X. Design of plasmonic comb-like filters using loop-based resonators. *Plasmonics* **2013**, *8*, 1017–1022. [CrossRef]

13. Al Mahmud, R.; Sagor, R.H.; Khan, M.Z.M. Surface plasmon refractive index biosensors: A review of optical fiber, multilayer 2D material and gratings, and MIM configurations. *Opt. Laser Technol.* **2023**, *159*, 108939. [CrossRef]
14. Zegaar, I.; Hocini, A.; Harhouz, A.; Khedrouche, D.; Salah, H.B. Design of a double-mode Plasmonic wavelength filter using a defective circular nano-disk resonator coupled to two MIM waveguides. *Prog. Electromagn. Res. Lett.* **2022**, *104*, 67–75. [CrossRef]
15. Luo, M.; Zhou, Y.; Zhao, X.; Li, Y.; Guo, Z.; Yang, X.; Zhang, M.; Wang, Y.; Wu, X. Label-Free Bound-States-in-the-Continuum Biosensors. *Biosensors* **2022**, *12*, 1120. [CrossRef] [PubMed]
16. Amrani, M.; Khattou, S.; Rezzouk, Y.; Mouadili, A.; Noual, A.; El Boudouti, E.H.; Djafari-Rouhani, B. Analytical and numerical study of T-shaped plasmonic demultiplexer based on Fano and induced transparency resonances. *J. Phys. D Appl. Phys.* **2021**, *55*, 075106. [CrossRef]
17. Karki, B.; Pal, A.; Sharma, S. Analysis of all-optical priority encoder using plasmonics waveguide. *J. Comput. Electron.* **2021**, *20*, 1884–1890. [CrossRef]
18. Wu, Y.; Zhao, X.; Hu, J.; Xu, H. Low threshold optical bistability based on coupled graphene Tamm states. *Results Phys.* **2021**, *21*, 103824. [CrossRef]
19. Chiam, S.Y.; Singh, R.; Rockstuhl, C.; Lederer, F.; Zhang, W.; Bettiol, A.A. Analogue of electromagnetically induced transparency in a terahertz metamaterial. *Phys. Rev. B* **2009**, *80*, 153103. [CrossRef]
20. Fano, U. Effects of configuration interaction on intensities and phase shifts. *Phys. Rev.* **1961**, *124*, 1866. [CrossRef]
21. Yang, X.; Hu, X.; Yang, H.; Gong, Q. Ultracompact all-optical logic gates based on nonlinear plasmonic nanocav-ities. *Nanophotonics* **2017**, *6*, 365–376. [CrossRef]
22. Chai, Z.; Hu, X.; Zhu, Y.; Sun, S.; Yang, H.; Gong, Q. Ultracompact chip-integrated electromagnetically induced transparency in a single plasmonic composite nanocavity. *Adv. Opt. Mater.* **2014**, *2*, 320–325. [CrossRef]
23. Kamada, S.; Okamoto, T.; El-Zohary, S.E.; Haraguchi, M. Design optimization and fabrication of Mach-Zehnder interferometer based on MIM plasmonic waveguides. *Opt. Express* **2016**, *24*, 16224–16231. [CrossRef] [PubMed]
24. Hsu, C.W.; Zhen, B.; Stone, A.D.; Joannopoulos, J.D.; Soljačić, M. Bound states in the continuum. *Nat. Rev. Mater.* **2016**,1, 16048.
25. Mesli, S.; Yala, H.; Hamidi, M.; BelKhir, A.; Baida, F.I. High performance for refractive index sensors via sym-metry-protected guided mode resonance. *Optics Express* **2021**, *29*, 21199–21211. [CrossRef] [PubMed]
26. Wang, Q.; Jiang, J.X.; Wang, L.; Yin, X.Y.; Yan, X.; Zhu, A.; Fengmei, Q.; Zhang, K.K. An asymmetric grating refractive index sensor generating quasi-bound states in the continuum with high figure of merit and temperature self-compensation. *J. Phys. D Appl. Phys.* **2022**, *55*, 155103. [CrossRef]
27. Maksimov, D.N.; Gerasimov, V.S.; Bogdanov, A.A.; Polyutov, S.P. Enhanced sensitivity of an all-dielectric refractive index sensor with an optical bound state in the continuum. *Phys. Rev. A* **2022**, *105*, 033518. [CrossRef]
28. Liang, Y.; Koshelev, K.; Zhang, F.; Lin, H.; Lin, S.; Wu, J.; Jia, B.; Kivshar, Y. Bound states in the continuum in anisotropic plasmonic metasurfaces. *Nano Lett.* **2020**, *20*, 6351–6356. [CrossRef]
29. Maksimov, D.N.; Gerasimov, V.S.; Romano, S.; Polyutov, S.P. Refractive index sensing with optical bound states in the continuum. *Opt. Express* **2020**, *28*, 38907–38916. [CrossRef]
30. Tang, S.; Chang, C.; Zhou, P.; Zou, Y. Numerical Study on a Bound State in the Continuum Assisted Plasmonic Refractive Index Sensor. *Photonics* **2022**, *9*, 224. [CrossRef]
31. Liu, X.; Li, F.; Li, Y.; Tang, T.; Liao, Y.; Lu, Y.; Wen, Q. Terahertz metasurfaces based on bound states in the continuum (BIC) for high-sensitivity refractive index sensing. *Optik* **2022**, *261*, 169248. [CrossRef]
32. Von Neumann, J.; Wigner, E.P. Über merkwürdige diskrete Eigenwerte. *Phys. Z.* **1929**, *30*, 465.
33. Sadrieva, Z.F.; Belyakov, M.A.; Balezin, M.A.; Kapitanova, P.V.; Nenasheva, E.A.; Sadreev, A.F.; Bogdanov, A.A. Experimental observation of a symmetry-protected bound state in the continuum in a chain of dielectric disks. *Phys. Rev. A* **2019**, *99*, 053804. [CrossRef]
34. Friedrich, H.; Wintgen, D. Interfering resonances and bound states in the continuum. *Phys. Rev. A* **1985**, *32*, 3231. [CrossRef]
35. Marinica, D.C.; Borisov, A.G.; Shabanov, S.V. Bound states in the continuum in photonics. *Phys. Rev. Lett.* **2008**, *100*, 183902.
36. Huang, L.; Jia, B.; Pilipchuk, A.S.; Chiang, Y.; Huang, S.; Li, J.; Miroshnichenko, A.E. General Framework of Bound States in the Continuum in an Open Acoustic Resonator. *Phys. Rev. Appl.* **2022**, *18*, 054021. [CrossRef]
37. Rybin, M.V.; Koshelev, K.L.; Sadrieva, Z.F.; Samusev, K.B.; Bogdanov, A.A.; Limonov, M.F.; Kivshar, Y.S. High-Q supercavity modes in subwavelength dielectric resonators. *Phys. Rev. Lett.* **2017**, *119*, 243901. [PubMed]
38. Chen, H.; Zhang, Z.; Zhang, X.; Han, Y.; Zhou, Z.; Yang, J. Multifunctional plasmon-induced transparency devices based on hybrid metamaterial-waveguide systems. *Nanomaterials* **2022**, *12*, 3273.
39. Rezzouk, Y.; El Ghafiani, M.; Khattou, S.; Amrani, M.; El Boudouti, E.H.; Talbi, A.; Djafari-Rouhani, B. High-Q Resonant Modes in Periodic Stubbed Structure. In Proceedings of the International Conference on Electronic Engineering and Renewable Energy Systems, Saidia, Morocco, 20–22 May 2022; Springer: Singapore, 2022; pp. 223–230
40. Koshelev, K.; Lepeshov, S.; Liu, M.; Bogdanov, A.; Kivshar, Y. Asymmetric metasurfaces with high-Q resonances governed by bound states in the continuum. *Phys. Rev. Lett.* **2018**, *121*, 193903.
41. Liu, Y.; Zhou, W.; Sun, Y. Optical refractive index sensing based on high-Q bound states in the continuum in free-space coupled photonic crystal slabs. *Sensors* **2017**, *17*, 1861. [CrossRef]

42. Wang, M.; Tian, H.; Liu, X.; Li, J.; Liu, Y. Multiparameter sensing based on tunable Fano resonances in MIM waveguide structure with square-ring and triangular cavities. *Photonics* **2022**, *9*, 291. [CrossRef]
43. Zafar, R.; Salim, M. Enhanced figure of merit in Fano resonance-based plasmonic refractive index sensor. *IEEE Sens. J.* **2015**, *15*, 6313–6317.
44. Wang, L.; Zeng, Y.P.; Wang, Z.Y.; Xia, X.P.; Liang, Q.Q. A refractive index sensor based on an analogy T shaped metal–insulator–metal waveguide. *Optik* **2018**, *172*, 1199–1204. [CrossRef]
45. Yi, X.; Tian, J.; Yang, R. Tunable Fano resonance in MDM stub waveguide coupled with a U-shaped cavity. *Eur. Phys. J. D* **2018**, *72*, 1–9. [CrossRef]
46. Adhikari, R.; Sbeah, Z.; Gupta, R.; Chauhan, D.; Nunzi, J.M.; Prakash Dwivedi, R. Compact and sensitive H-shaped metal–dielectric–metal waveguide plasmonic sensor. *Plasmonics* **2022**, *17*, 1593-1606.
47. Kazanskiy, N.L.; Khonina, S.N.; Butt, M.A. Plasmonic sensors based on Metal-insulator-metal waveguides for re-fractive index sensing applications: A brief review. Physica E Low Dimens. *Syst. Nanostruct.* **2020**, *117*, 113798.
48. Hassan, M.F.; Sagor, R.H.; Amin, M.R.; Islam, M.R.; Alam, M.S. Point of care detection of blood electrolytes and glucose utilizing nano-dot enhanced plasmonic biosensor. *IEEE Sens. J.* **2021**, *21*, 17749–17757.
49. Rohimah, S.; Tian, H.; Wang, J.; Chen, J.; Li, J.; Liu, X.; Cui, J.; Hao, Y. Tunable multiple Fano resonances based on a plasmonic metal-insulator-metal structure for nano-sensing and plasma blood sensing applications. *Appl. Opt.* **2022**, 61, 1275–1283.
50. Chen, J.; Lian, X.; Zhao, M.; Xie, C. Multimode Fano Resonances Sensing Based on a Non-Through MIM Waveguide with a Square Split-Ring Resonance Cavity. *Biosensors* **2022**, *12*, 306. [CrossRef]
51. Karki, B.; Vasudevan, B.; Uniyal, A.; Pal, A.; Srivastava, V. Hemoglobin detection in blood samples using a gra-phene-based surface plasmon resonance biosensor. *Optik* **2022**, *270*, 169947.
52. Singh, R.R.; Kumari, S.; Gautam, A.; Priye, V. Glucose sensing using slot waveguide-based SOI ring resonator. *IEEE J. Sel. Top Quantum. Electron.* **2018**, *25*, 1–8. [CrossRef]
53. Amrani, M.; Khattou, S.; El Boudouti, E.H.; Talbi, A.; Akjouj, A.; Dobrzynski, L.; Djafari-Rouhani, B. Frie-drich-Wintgen bound states in the continuum and induced resonances in a loop laterally coupled to a waveguide. *Phys. Rev. B* **2022**, *106*, 125414. [CrossRef]
54. Zhou, T.; Gou, X.; Xu, W.; Li, Y.; Zhai, X.; Li, H.; Wang, L. Dynamically tunable plasmon-induced transparency in a T-shaped cavity waveguide based on bulk Dirac semimetals. *Plasmonics* **2021**, *16*, 323-332.
55. Kamari, M.; Hayati, M.; Khosravi, S. Tunable infrared wide band-stop plasmonic filter using T-shaped resonators. *Mater. Sci. Semicond.* **2021**, *133*, 105983.
56. Dobrzynski, L.; Akjouj, A.; El Boudouti, E.H.; Lèveque, G.; Al-Wahsh, H.; Pennec, Y.; Ghouila-Houri, C.; Talbi, A.; Djafari-Rouhani, B.; Jin, Y. *Photonics*; Elsevier: Amsterdam, The Netherlands, 2020.
57. Yang, H.U.; D'Archangel, J.; Sundheimer, M.L.; Tucker, E.; Boreman, G.D.; Raschke, M.B. Optical dielectric function of silver. *Phys. Rev. B* **2015**, *91*, 235137. [CrossRef]
58. Niu, L.; Xiang, Y.; Luo, W.; Cai, W.; Qi, J.; Zhang, X.; Xu, J. Nanofocusing of the free-space optical energy with plasmonic Tamm states. *Sci. Rep.* **2016**, *6*, 39125. [PubMed]
59. Naghizadeh, S.; Kocabaş, Ş.E. Guidelines for designing 2D and 3D plasmonic stub resonators. *J. Opt. Soc. Am. B* **2017**, *34*, 207–217. [CrossRef]
60. Zhang, K.; Li, D.; Chang, K.; Zhang, K.; Li, D. *Electromagnetic Theory for Microwaves and Optoelectronics*; Springer: Berlin/Heidelberg, Germany, 2008.
61. Djafari-Rouhani, B.; El Boudouti, E.H.; Akjouj, A.; Dobrzynski, L.; Vasseur, J.O.; Mir, A.; Fettouhi, N.; Zemmouri, J. Surface states in one-dimensional photonic band gap structures. *Vacuum* **2001**, *63*, 177–183.
62. Rezzouk, Y.; Amrani, M.; Khattou, S.; El Boudouti, E.H.; Djafari-Rouhani, B. Plasmonic Tamm states in periodic stubbed MIM waveguides: Analytical and numerical study. *JOSA B* **2022**, *3*, 600–610.
63. White, I.M.; Fan, X. On the performance quantification of resonant refractive index sensors. *Opt. Express* **2008**, *16*, 1020–1028. [CrossRef]
64. Bria, D.; Djafari-Rouhani, B.; Akjouj, A.; Dobrzynski, L.; Vigneron, J.P.; El Boudouti, E.H.; Nougaoui, A. Band structure and omnidirectional photonic band gap in lamellar structures with left-handed materials. *Phys. Rev. E 69* **2004**, *69*, 066613. [CrossRef]
65. Gollub, J.N.; Smith, D.R.; Vier, D.C.; Perram, T.; Mock, J.J. Experimental characterization of magnetic surface plasmons on metamaterials with negative permeability. *Phys. Rev. B* **2005**, *7*, 195402. [CrossRef]
66. Liu, S.; Du, J.; Lin, Z.; Wu, R.X.; Chui, S.T. Formation of robust and completely tunable resonant photonic band gaps. *Phy. Rev. B* **2008**, *78*, 155101.
67. Liu, S.; Lu, W.; Lin, Z.; Chui, S.T. Magnetically controllable unidirectional electromagnetic waveguiding devices designed with metamaterials. *Appl. Phys. Lett.* **2010**, *97*, 20. [CrossRef]
68. Zhao, L.; Wen, G.; Zhang, L.; Tong, J.; You, Y.; Ba, Q.; Luo, Q.; Liu, S. Reconfigurable unidirectional propagation of electromagnetic waves in photonic crystal waveguides. *JOSA B* **2022**, *39*, 2443–2449. [CrossRef]
69. Chai, Z.; Hu, X.; Yang, H.; Gong, Q. Chip-integrated all-optical diode based on nonlinear plasmonic nanocavities covered with multicomponent nanocomposite. *Nanophotonics* **2017**, *6*, 329–339. [CrossRef]

70. Bozhevolnyi, S.I.; Volkov, V.S.; Devaux, E.; Laluet, J.Y.; Ebbesen, T.W. Channel plasmon subwavelength waveguide components including interferometers and ring resonators. *Nature* **2006**, *440*, 508–511. [CrossRef]
71. Johnson, P.B.; Christy, R.W. Optical constants of the noble metals. *Phys. Rev. B* **1972**, *6*, 4370. [CrossRef]